Expanded Phase Distribution in Low Average Layer-Number 2D Perovskite Films: Toward Efficient Semitransparent Solar Cells

Yi Yang, Cheng Liu, Hiroyuki Kanda, Yong Ding,* Hao Huang, Haibin Chen, Bin Ding, Yongri Liang, Xuepeng Liu, Molang Cai, Paul J. Dyson,* Songyuan Dai,* and Mohammad Khaja Nazeeruddin*

The application of low average layer-number ($\langle n \rangle \leq 2$) 2D perovskites in semitransparent photovoltaics (ST-PVs) has been hindered by their strong exciton binding energy and high electrical anisotropy. Here, the phase distribution is expanded fully and orderly to enable efficient charge transport in 2D $(NMA)_2(MA)Pb_2I_7$ (NMA: 1-naphthylmethylammonium, MA: $CH_3NH_3^+$) perovskite films by regulating the sedimentation dynamics of organic cation-based colloids. Ammonium chloride is synergistically introduced to enhance the phase separation further and construct a favorable out-of-plane orientation. The wide and graded phase distribution well aligns the energy level to facilitate charge transfer. As a result, the first application of an average $\langle n \rangle = 2$ 2D perovskite is implemented in ST-PVs with visible power conversion efficiency (PCE) of 7.52% and high average visible transmittance (AVT) of 40.5%. This study offers a new candidate and an effective strategy for efficient and stable ST-PVs and is relevant to other perovskite optoelectronic devices.

1. Introduction

Semitransparent photovoltaic (ST-PV) technologies have generated enormous research interest due to their promising applications in building-integrated photovoltaics,[1] automobiles,[2] and tandem devices,[3] which can, in principle, compensate for half of the current world's energy consumption.[4,5] However, the unaesthetic issue of Si ST-PVs and the relatively low efficiency of organic polymer ST-PVs prohibit their large-scale applications.[6] Perovskites (typically $APbX_3$, with A-site monovalent cations and X-site halide anions) embrace a unique set of attractive properties, such as large absorption coefficients,[7] facilely tunable bandgap,[8] high charge carrier mobilities,[9] and various deposition protocols,[10] and consequently have been identified as ideal semiconductor candidates for ST applications.[11]

To obtain highly transparent perovskite films, recent findings offer a range of solutions: i) coverage reduction,[12] ii) thickness decrease,[13] iii) microstructure adjustment,[14] and iv) bandgap tuning.[15] Even so, the power conversion efficiencies (PCEs) of these ST perovskite solar cells (PSCs) with average visible transmittances (AVTs) over 40% are still negligible due to their inevitable shortcomings, such as poor coverage, damaged morphology, high trap densities, or heavy light loss.[5,15] Moreover, the easy decomposition of 3D perovskites under harsh conditions brings about inferior operating stabilities for ST-PSCs, which is another crucial hurdle prior to their practical application.[16,17]

Two-dimensional (2D) perovskites formed by incorporating bulky organic cations at the A site show enormous potential for application in ST-PSCs due to their flexible color tunability and superior ambient stability.[18,19] By slicing the perovskite crystallographic plane with large insulating organic spacer cations, the inorganic slabs of metal halide octahedra are separated and species with different layer thickness (n value) are thereby produced.[20] Typical 2D perovskite films comprise multiple phases with varying n values because of their diverse formation energy, hence the average layer thickness is defined as $\langle n \rangle$ value according to the precursor stoichiometry to judge the perovskite dimension.[21] The low average layer-number 2D

Y. Yang, C. Liu, Dr. Y. Ding, Dr. X. Liu, Prof. M. Cai, Prof. S. Dai
State Key Laboratory of Alternate Electrical Power System with Renewable Energy Sources
North China Electric Power University
Beijing 102206, P. R. China
E-mail: dingy@ncepu.edu.cn; sydai@ncepu.edu.cn
Y. Yang, C. Liu, Dr. H. Kanda, Dr. Y. Ding, Dr. B. Ding, Prof. P. J. Dyson, Prof. M. K. Nazeeruddin
Institute of Chemical Sciences and Engineering
EPFL Valais
Sion 1951, Switzerland
E-mail: paul.dyson@epfl.ch; mdkhaja.nazeeruddin@epfl.ch
H. Huang, Dr. H. Chen
Hebei Key Lab of Optic-Electronic Information and Materials
College of Physics Science and Technology
Hebei University
Baoding 071002, China
Prof. Y. Liang
State Key Lab of Metastable Materials Science and Technology, and College of Materials Science and Engineering
Yanshan University
No. 438 West Hebei Avenue, Qinhuangdao, Hebei 066004, P. R. China

The ORCID identification number(s) for the author(s) of this article can be found under https://doi.org/10.1002/adfm.202104868.
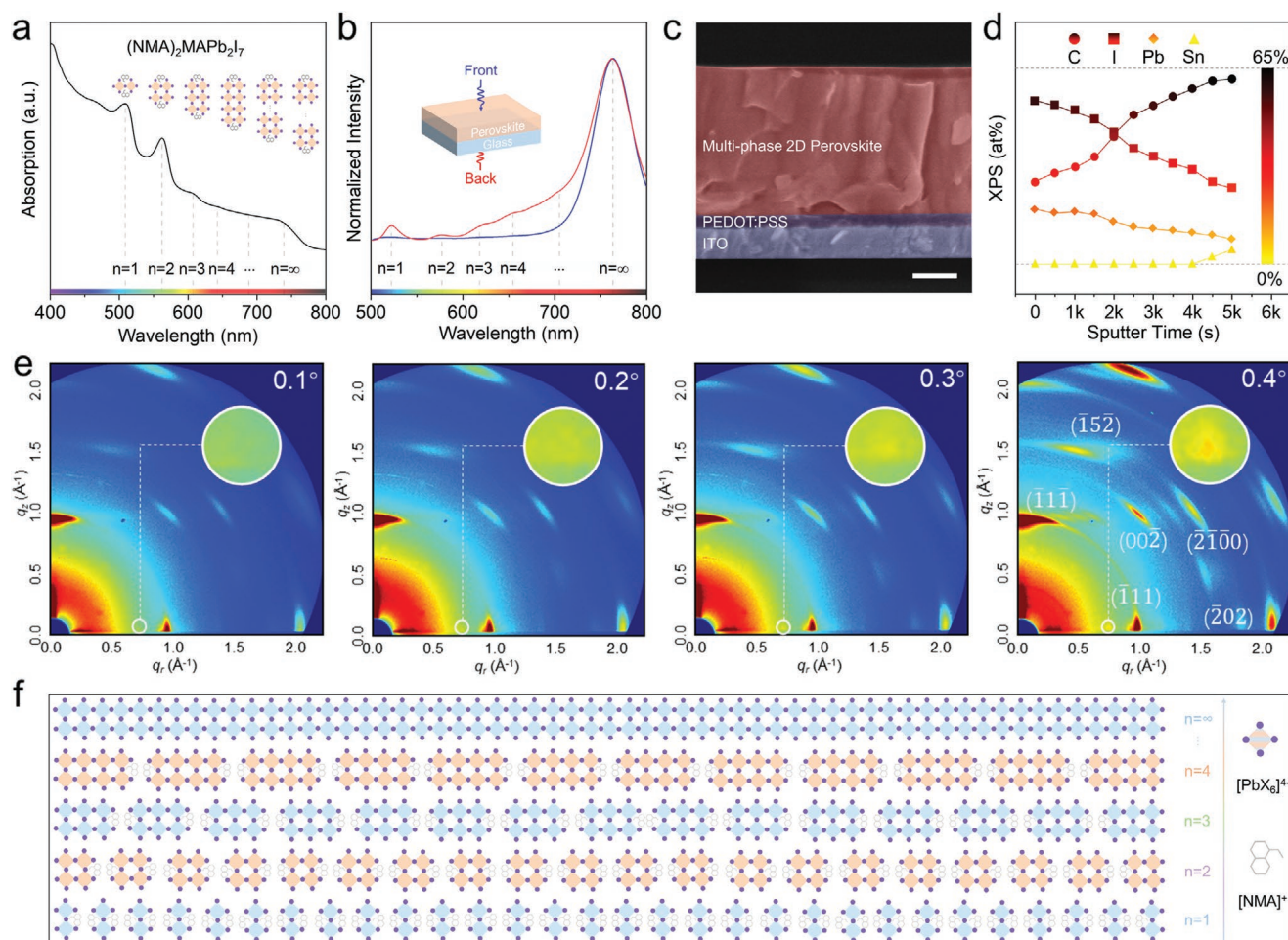
Figure 1. Phase Distribution Characterizations. a) UV–vis spectrum, b) PL spectra excited from the film (front) and glass (back) side, c) cross-sectional scanning electron microscope (SEM) image, scale bar: 200 nm, d) XPS depth profile analysis, e) GIWAXS images with the incidence angles changing from 0.1°, 0.2°, 0.3°, and 0.4°, and f) schematic illustration of the proposed phase distribution of the $(NMA)_2(MA)Pb_2I_7$ film.

($\langle n \rangle \leq 2$) perovskite exhibits large bandgaps, high AVTs, and excellent stability, which are especially favored by ST-PSCs. However, these highly transparent 2D PSCs show PCEs only around 3% to date.[22,23] One reason is that the out-of-plane charge transport is hindered by the high electrically anisotropic structure.[24–27] The other arises from the narrow quantum-well structure, where the strong Coulombic interactions enhance the exciton binding energy and impedes charge separation.[20,24] Therefore, the unreconciled conflict between AVTs and PCEs impedes the potential advantage of 2D perovskites for next-generation ST-PV applications.

In this work, we report both highly transparent and efficient ST-PSCs by using a novel 2D perovskite $(NMA)_2(MA)Pb_2I_7$ ($\langle n \rangle$ = 2 according to the precursor stoichiometry, NMA: 1-naphthylmethylammonium, MA: $CH_3NH_3^+$). The sedimentation dynamics of the organic cation-based colloids are regulated to fully expand the phase distribution (n = 1, 2, ..., ∞) for the low average layer-number 2D perovskite films with n value gradually increasing from the bottom to top. Ammonium chloride (NH_4Cl) is additionally employed to further enhance the phase separation and promote the favorable out-of-plane orientation. The wide and graded phase distribution successfully overcomes

the limitation of the narrow quantum-well structure, aligns the energy level, and enables fluent charge transport in the vertically oriented 2D perovskite films. As a result, we implement the first application of an $\langle n \rangle$ = 2 2D perovskite (according to the precursor stoichiometry) in ST-PVs with a visible PCE of 7.52% and a high AVT of 40.5%. This work demonstrates an effective strategy of enabling efficient solar cells using low average layer-number 2D perovskites and offers a new candidate for efficient and stable ST-PVs and other perovskite optoelectronic devices.

2. Results and Discussion

The 2D $(NMA)_2(MA)Pb_2I_7$ ($\langle n \rangle$ = 2 according to the precursor stoichiometry) perovskite films were prepared through an NH_4Cl-assisted one-step solution deposition method.[26] To determine the phase composition of the 2D perovskite film, ultraviolet-visible (UV-vis) spectroscopy was first conducted. As shown in **Figure 1**a, multiple short-wavelength excitonic absorption peaks and an absorption onset at around 775 nm were observed, indicating the coexistence of multiple phases with n varying from 1 to ∞ in the 2D perovskite film.[28] The observed absorption peak

at ≈510 nm corresponds well with the optical characteristics of the pure 2D perovskite as shown in Figure S1 (Supporting Information). It is worth noting that this obvious phase separation in the $\langle n \rangle = 2$ 2D perovskite film is very different from that of the previous studies, which normally reported purer phase composition.[29,30] Steady-state photoluminescence (PL) spectra were performed with an excitation wavelength at 450 nm from both front side and back side to preliminarily explore the vertical phase distribution (Figure 1b). Apart from the dominant luminescence peak at ≈764 nm in both excitation cases, additional higher-energy peaks at ≈524, 577, 620, and 656 nm appear when excited from the back side, suggesting the high n value phases are favored at the film surface whereas the low n value phases tend to locate at the bottom.[31] From the final composition point of view, the $n = 2$ phase is not dominant. It seems that the bottom lower layer-number ($n = 1$–4) phases and the upper multiple higher layer-number phases compose the final mixed-dimensional perovskite film. This vertical multi-phase distribution can hardly be recognized from the cross-sectional morphology (Figure 1c), while it should be reflected on the element distribution. Depth profile X-ray photoelectron spectroscopy (XPS) was used to reveal the change in film composition in the vertical direction (Figure 1d). The detected C signal is governed by the amount of bulky organic spacer cations and the I/Pb ratio depends on the layer thickness of inorganic slabs. As the sputtering time prolongs, the percentage of C atoms gradually increases while the I/Pb ratio shows a continuous downward trend, demonstrating the n value constantly decreases from the perovskite film surface to the bottom.

This difference was also verified by the grazing-incidence wide-angle X-ray scattering (GIWAXS) measurement. The depth-sensitive crystallographic information can be provided by increasing the incidence angle. The GIWAXS penetration depth was calculated at each angle as shown in Figure S2 (Supporting Information). For angles below the critical angle 0.2°, the X-rays detect only the film surface within several tens of nanometers, where the $(NMA)_2(MA)Pb_2I_7$ film exhibits an out-of-plane orientation with sharp, discrete Bragg spots assigned to the oriented high layer-number 2D perovskite or 3D-like components (Figure 1e). When the incidence angle increases to 0.4°, an additional peak at $q \approx 0.7$ Å^{-1} is observed along the q_r axis, indicative of oriented $n = 1$ 2D phase (Figure S3a, Supporting Information) in the deeper region of the perovskite film.[32] The 2D GIWAXS patterns are consistent with the XRD results as shown in Figures S3 and S4 (Supporting Information). The $(NMA)_2(MA)Pb_2I_7$ film exhibits dominant (111) and (202) reflections at 14.3° and 28.6°, which were normally observed in quasi-2D perovskites with $\langle n \rangle \geq 3$, rather than characteristic (0k0) reflections as reported in n-butylammonium (BA)- and phenylethylammonium (PEA)-based 2D perovskites with $\langle n \rangle = 2$.[33] This is because the final $(NMA)_2(MA)Pb_2I_7$ film is a graded structure with mixed dimensional phases, and the $n = 2$ component is in the minority. This is also the unique feature of the NMA cation which we took advantage of. The low diffraction angle peaks at around 4.9° and 9.8° are indexed as the (002) and (004) crystal planes of the $n = 1$ NMA$_2$PbI$_4$ perovskite, confirming the phase separation.[34] Based on these observations, the distribution of multiple perovskite phases throughout the whole bulk film is illustrated in Figure 1f.

The graded $(NMA)_2(MA)Pb_2I_7$ film is composed of high n value 3D-like phase governing the upper regions and the 2D phases with gradually decreased n value dominating the deeper regions, which is expected to improve the energy alignment and charge transfer in p-i-n configuration.

Ultrafast transient absorption (TA) spectroscopy was carried out on the 2D perovskite films with $\langle n \rangle = 2$ to investigate the phase distribution behavior using different organic spacer cations. Upon a 2.48 eV photon pulse excitation, the $(BA)_2(MA)Pb_2I_7$, $(PEA)_2(MA)Pb_2I_7$, and $(NMA)_2(MA)Pb_2I_7$ perovskite films demonstrate their ground state bleaching (GSB) signals as shown in **Figure 2**a. The $(BA)_2(MA)Pb_2I_7$ film displays only two GSB peaks of $n = 2$ and 3 with an energy distribution (ΔE) of 0.13 eV. As the spacer cation size increases, the $(PEA)_2(MA)Pb_2I_7$ film exhibits more GSB peaks ascribed to the phases of $n = 1, 2, 3, 4,$ and 5 as well as a larger ΔE of 0.54 eV. Notably, the TA spectra of the $(NMA)_2(MA)Pb_2I_7$ film is featured by the continuous GSB peaks of $n = 1, 2, 3, 4, 5, \ldots \infty$ at 2.42, 2.18, 2.02, 1.92, 1.84, ... 1.65 eV, respectively, and an ΔE as high as 0.77 eV. Therefore, enlarging the organic spacer cation significantly broadens the phase distribution of the 2D perovskite film. Besides, the evolution of the GSB signal reduction at higher energies (lower n value phases) is accompanied with the enhancement of GSB peaks at lower energies (higher n value phases), suggesting the charge transfer among these phases.[28,31]

Detailed carrier dynamics of the $(NMA)_2(MA)Pb_2I_7$ film were analyzed by the time-resolved TA spectra (Figure 2b). The $n = 1$ bleaching starts at 0.3 ps, followed by an ultrafast decay. When the n value increases, the bleaching onset is gradually delayed and the decay time is considerably prolonged, especially for the $n = \infty$, revealing a fast charge transfer from low to high n value phases in the 2D perovskite (Figure 2c). This trend is also reflected in the PL decay kinetics of the $n = 2$ emission at 577 nm. The fast decay lifetime τ_1 for the three perovskite films on poly(3,4-ethylenedioxythiophene):poly(styrenesulfonate) (PEDOT:PSS) substrates are compared in Figure S5 and Table S1 (Supporting Information). The shorter τ_1 for the $(NMA)_2(MA)Pb_2I_7$ sample proves that the accumulation of low n value phases in the bottom region can efficiently promote the transfer of photogenerated holes across the perovskite film and their following injection to the PEDOT:PSS layers.[35] It is noted that the $(BA)_2(MA)Pb_2I_7$ and $(PEA)_2(MA)Pb_2I_7$ films also exhibit short lifetimes which may result from their pretty poor morphology (Figure S6, Supporting Information) and the consequent charge recombination.[8] PL intensity map (Figure 2d) of the $(NMA)_2(MA)Pb_2I_7$ sample also shows least radiative recombination with the lowest average emission intensity, which well confirms the improved charge transport in the perovskite film and the accelerated charge extraction at the interface. In addition, more homogeneous emission of the $(NMA)_2(MA)Pb_2I_7$ sample may imply less defects existing in the graded 2D perovskite film.[36] To verify this hypothesis, we quantified the trap density of states (tDOS) of 2D perovskite films through the thermal admittance spectroscopy (TAS). As shown in Figure 2e, the $(NMA)_2(MA)Pb_2I_7$ film presents much lower tDOS especially in the deeper energy region (0.40–0.50 eV) which is assigned to the traps at film surface.[37] Combined with the top-view SEM images of these 2D perovskite films (Figure S6, Supporting Information), we can conclude that the ordered phase distribution facilitates the formation of more continuous
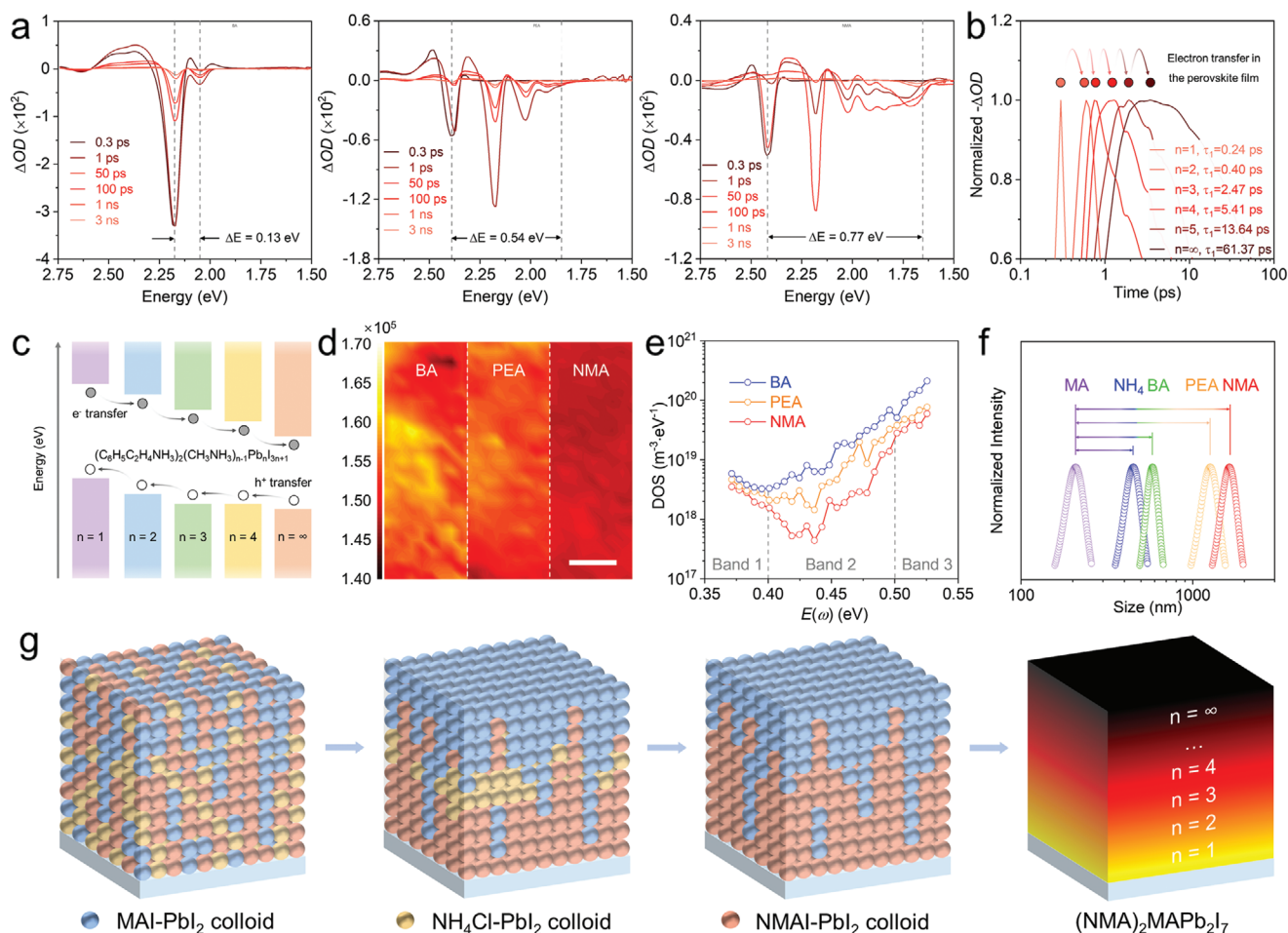
Figure 2. Mechanism of the Wide and Graded Phase Distribution. a) The TA spectra at specific delay times of different 2D perovskite films. b) TA kinetics extracted from different GSB ($n = 1, 2, 3, 4, 5, \infty$). c) Schematic of the internal electron/hole transfer among different phases. d) PL intensity maps integrated from 700–800 nm of the 2D perovskite films on PEDOT:PSS substrates. Scale bar, 1 µm. e) The tDOS distribution of different 2D PSCs. f) DLS results showing the colloid size distribution in precursor solutions. g) Schematic diagrams indicating the formation of the wide and graded 2D perovskite film.

and uniform film surface mainly consisting of high n value phases, which would minimize the defect densities in the perovskite layers and the trap-assisted carrier recombination in the photovoltaic devices.

In principle, the wide and graded phase distribution of the 2D perovskite film essentially depends on the spatial distribution of organic cations in the precursor solution. Moreover, the organic cations are normally in the form of colloids by micellization with other components after dissolution.[38] Thus, it is reasonable to speculate that the polydispersity of n values is related to the colloidal properties. We thereby conducted the dynamic light scattering (DLS) on perovskite precursor solutions based on different organic cations. Considering the incorporation of NH$_4$Cl additive, we also compare the colloidal property of the NH$_4$-based perovskite precursor solution to estimate its impact on the spatial distribution of organic cations. As shown in Figure 2f, the NMA-based clusters have a much larger average colloidal size of ≈1626 nm, followed by PEA-based clusters of ≈1257 nm, BA-based clusters of ≈585 nm, NH$_4$-based clusters of ≈448 nm, and then MA-based clusters of ≈207 nm. The

Tyndall effect photographs of these perovskite precursors are consistent with the DLS results as indicated in Figure S7 (Supporting Information). Presently, the classical sedimentation model has been used to broadly describe the heterogeneous dispersed system.[39] In the gravitational field, smaller colloidal particles have relatively lower sedimentation rates and require longer time to reach the sedimentation equilibrium, because the sedimentation effect is offset by the Brownian motion-induced diffusion. While the Brownian motion can be overcome by the gravitational field of larger colloidal particles, which will settle to the bottom at a higher sedimentation rate and quickly establish the sedimentation equilibrium status.[40] During the spin-coating of the NH$_4$Cl-containing (NMA)$_2$(MA)Pb$_2$I$_7$ precursor solution, the sedimentation sequence should be as follows: first NMA-based clusters, then NH$_4$-based clusters, and last MA-based clusters. As a result, NMA-based clusters with preferential sedimentation would show higher concentrations closer to the substrate (Figure 2g), followed by NH$_4$-based clusters in the middle, whereas MA-based clusters with the slowest sedimentation would dominate the top region. The NH$_4$-based

**ADVANCED
SCIENCE NEWS**

www.advancedsciencenews.com

**ADVANCED
FUNCTIONAL
MATERIALS**

www.afm-journal.de

clusters divide the two regions and increase their physical distance, thus further separating the MA and NMA regions. During the film formation, NH_4^+ would gradually deprotonate and escape from the film in annealing under humidity as we previously reported.[26] Therefore, the special spatial distribution of MA^+ and NMA^+ eventually contributes to a graded 2D perovskite film with the lower-n component at the bottom and the higher-n component on the surface. And NH_4^+ further enhances the degree of this phase separation as confirmed by the UV-vis and PL spectra (Figure S8, Supporting Information). The difference in average colloidal size between the bulkier cation and MA^+ is responsible for the graded structure, which explains the narrower phase distribution in $(PEA)_2(MA)Pb_2I_7$ and the nearly pure phase in $(BA)_2(MA)Pb_2I_7$ (Figure S9, Supporting Information). To verify the proposed mechanism, the phase distribution in the $(NMA)_2CsPb_2I_7$ film was further investigated. Since the difference in the average colloidal sizes between Cs- and NMA-based clusters is smaller than that between MA- and NMA-based clusters (Figure S10a, Supporting Information), a lower degree of phase separation can be expected in the $(NMA)_2CsPb_2I_7$ film. As shown in Figure S10b (Supporting Information), a dominant excitonic absorption peak at ≈555 nm together with a minor peak at ≈596 nm was observed, which are assigned to the $n = 2$ and $n = 3$ phases, respectively.[41] Thus, the formation of high n value phases is significantly suppressed and the phase

distribution is concentrated in the $(NMA)_2CsPb_2I_7$ film compared to the $(NMA)_2(MA)Pb_2I_7$ film, confirming that the phase distribution behavior is closely related to the precursor colloidal properties.

Besides affecting the phase distribution, NH_4Cl also plays a role in promoting the out-of-plane orientation of 2D perovskite films. As shown in Figure S11 (Supporting Information), the $(NMA)_2(MA)Pb_2I_7$ film without NH_4Cl exhibits a random orientation compared to the significantly enhanced out-of-plane orientation of the NH_4Cl-incorporated film (Figure 1e). Meanwhile, larger-size column-like crystal grains were achieved by using NH_4Cl (Figure S12, Supporting Information). As we previously reported, the specific adsorption of NH_4Cl on the (202) crystal plane, together with the subsequent deprotonation of NH_4^+ under humidity and heat guided the out-of-plane crystal growth of 2D perovskites.[26,37] Thus, the NH_4Cl is not expected to exist in the final film but takes effects in the film formation process for enhancing the phase separation and the preferential orientation of 2D perovskites, which is favorable for high carrier mobility and low trap state density (Figure S13, Supporting Information).[26]

Besides favorable electrical properties, the graded 2D perovskite film is also expected to possess a significantly enhanced optical transparency compared to the 3D analogue due to the decreased absorption coefficient with the reduction of n value (**Figure 3**a).[42] Thus, a 2D perovskite film owing both the lowest
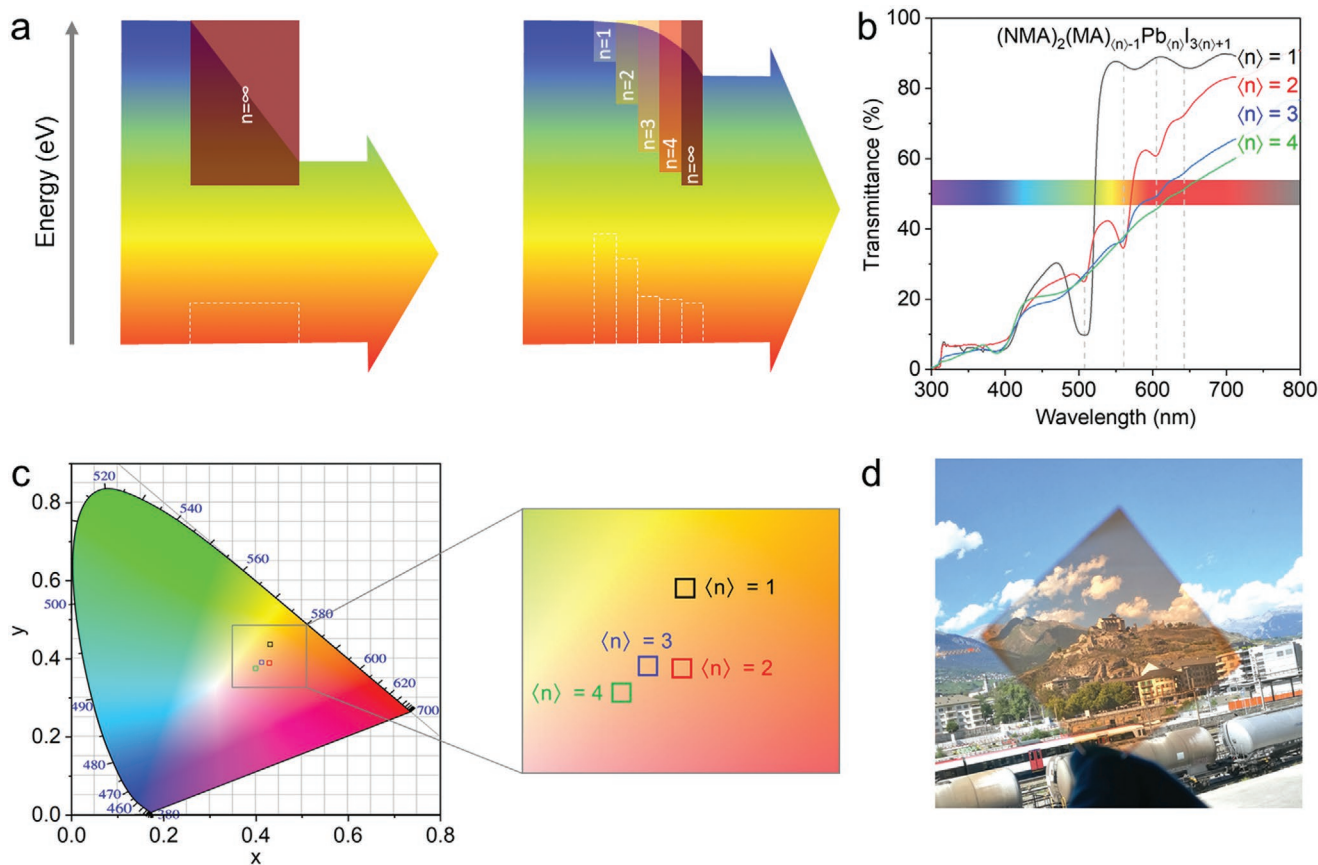

Figure 3. Optical Properties of the 2D Perovskite Films. a) Schematic illustration showing the light harvesting of 3D and graded 2D perovskite films. b) Transmission spectra of $(NMA)_2(MA)_{\langle n\rangle-1}Pb_{\langle n\rangle}I_{3\langle n\rangle+1}$ films. c) Color coordinates of the $(NMA)_2(MA)_{\langle n\rangle-1}Pb_{\langle n\rangle}I_{3\langle n\rangle+1}$ films plotted on the CIE 1931xyY chromaticity diagram. The inset is the photograph of 2D perovskite film with $\langle n\rangle = 2$. d) Photographs of the semitransparent $(NMA)_2(MA)Pb_2I_7$ film.

**ADVANCED
SCIENCE NEWS**

www.advancedsciencenews.com

**ADVANCED
FUNCTIONAL
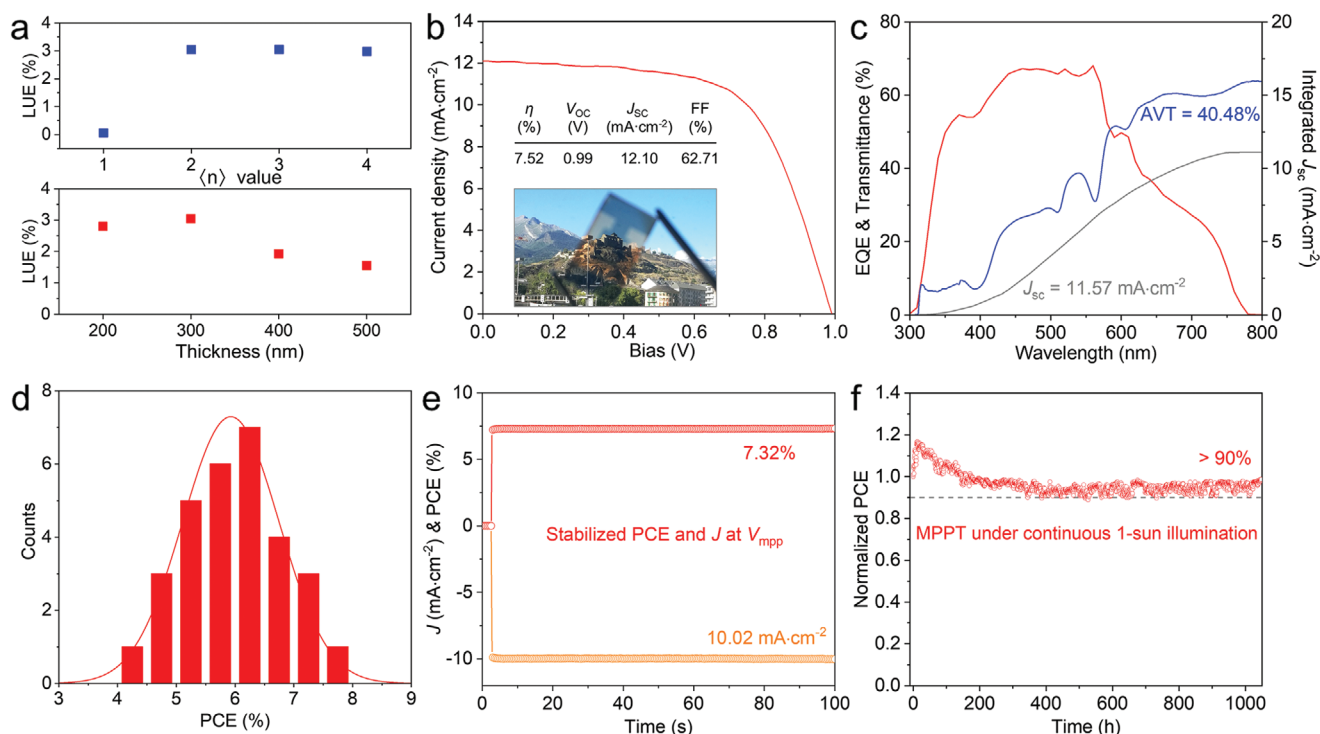MATERIALS**

www.afm-journal.de

Figure 4. Photovoltaic Performance of Semitransparent 2D PSCs. a) The device LUE as a function of the *n* value and film thickness. b) The *J–V* characteristics of the best-performing device. The inset is the photograph of the semitransparent device. c) The transmission spectrum, EQE, and the integrated J_{SC} of the best device. d) Histogram of the device efficiency for 30 devices. e) The steady-state output of the device measured under the V_{mpp} of 0.73 V. f) The maximum power point tracking (MPPT) of the unencapsulated device under continuous 1 sun illumination.

possible ⟨*n*⟩ value and graded multi-phase distribution should be regarded as a promising light-absorber for ST-PV applications. The optical properties of the $(NMA)_2(MA)_{⟨n⟩−1}Pb_{⟨n⟩}I_{3⟨n⟩+1}$ 2D perovskite films were investigated by the transmittance spectra (Figure 3b). The AVTs in the visible light range (380–780 nm) were calculated using the generally accepted approach:[4]

$$\text{AVT} = \frac{\int T(\lambda)P(\lambda)S(\lambda)d(\lambda)}{\int P(\lambda)S(\lambda)d(\lambda)} \qquad (1)$$

where *T*, *λ*, and *P* are the transmission, wavelength and photopic response, respectively. *S* corresponds to the solar photon flux (AM1.5G). The NMA_2PbI_4 film shows the highest AVT of about 73% but the single-phase component and ultra-high exciton binding energy block their application in solar cells.[43] Unlike other ⟨*n*⟩ = 2 2D perovskites, the $(NMA)_2(MA)Pb_2I_7$ film not only achieves a high AVT of around 47% but also realizes a graded phase structure, which meets the requirements of ST-PVs. Since human visual color perception is also an important factor for evaluating the color-rendering property of ST-PVs,[44,45] the color coordinates (*x*, *y*) were calculated and reflected on the CIE 1931 chromaticity diagram. As shown in Figure 3c,d, the $(NMA)_2(MA)Pb_2I_7$ film exhibits a nice orangish color perceived by human eyes, demonstrating an appealing color appearance for architectural design.

The semitransparent 2D PSCs were fabricated to evaluate the photovoltaic performance with a configuration of indium-doped

tin oxide (ITO)/PEDOT:PSS/2D perovskites/[6,6]-phenyl-C61-butyric acid methyl ester (PCBM)/bathocuproine (BCP)/Ag. In order to maximize the device transparency and performance, we optimized the light utilization efficiency (LUE) by tuning the ⟨*n*⟩ value and the film thickness (**Figure 4**a). LUE is defined as the product of PCE and AVT.[5] The increase of *n* value and film thickness, the PCEs improve while the AVTs reduce (Figure S14 and Table S2, Supporting Information). The highest LUE was achieved by the 300 nm-thick $(NMA)_2(MA)Pb_2I_7$ film. Figure 4b displays the current density–voltage (*J–V*) characteristics of the champion device with an open-circuit voltage (V_{OC}) of 0.99 V, short-circuit current density (J_{SC}) of 12.10 mA cm⁻² and fill factor (FF) of 62.17%, resulting in a PCE up to 7.52% with negligible hysteresis (Table S3, Supporting Information). The V_{OC} is lower than expected for this material, which may be caused by the imperfect morphology and the related non-radiative carrier recombination (Figure S12, Supporting Information).[7] The relatively high efficiency for such low average layer-number 2D PSCs benefits from the fluent carrier transport/extraction dredged by the graded energy alignment and the favorable out-of-plane orientation. Encouragingly, this device is also visually transparent (inset of Figure 4b), which exhibits an AVT as high as 40.48% (Figure 4c). The resultant LUE of 3.04% achieved in this work is one of the best LUE values reported for semitransparent PSCs so far (Table S4, Supporting Information), demonstrating the great potential of this 2D perovskite material for application in ST-PVs. To further investigate the photon-electron conversion characteristics, the external quantum efficiency

(EQE) spectrum was performed (Figure 4c). The relatively weak spectral response to lower energy photons indicates the limited 3D-like phases in the perovskite film, corresponding to the high transmittance at long wavelengths. Whereas a strong spectral response was observed at short wavelengths demonstrating that the high-energy-sensitive low-dimensional phases substantially contribute to the photon-electron conversion. Benefiting from the well-aligned phases, a high integrated J_{SC} of 11.57 mA cm^{-2} was eventually achieved matching that obtained from the J–V measurements. To evaluate the reproductivity, 30 devices were prepared independently under the same condition (Figure 4d). The PCE histogram shows that over 50% of the devices have efficiencies exceeding 6% with an average PCE of 6.61%. The stabilized photocurrent as a function of time was also recorded at the maximum power point voltage (V_{mpp}) of 0.73 V, which immediately reached $\approx$ 10.02 mA cm^{-2} upon illumination, leading to a steady-state PCE of 7.32% (Figure 4e). With the achieved satisfying photovoltaic performance, we examined the device operational stability under continuous one sun illumination (AM1.5G) in a nitrogen atmosphere. Figure 4f depicts the normalized PCE evolution over time of the unencapsulated device traced at the maximum power point (MPP). The $(NMA)_2(MA)Pb_2I_7$-based ST-PV maintains 90% of its initial efficiency after 1000 h of continuous operation, which is to our knowledge one of the best stabilities achieved by 2D PSCs at the MPP for over 1000 h.[27,46] Moreover, the unsealed device maintains 92.5% of its initial efficiency after aging 312 h under ambient of $\approx$40–50% relative humidity at room temperature in the dark (Figure S15, Supporting Information), indicating that it retains the advantage of good ambient stability of 2D perovskites. Such robust stability mainly stems from the hydrophobicity of the naphthyl cation, the blocked ion migration within the 2D perovskite lattice,[47,48] and the highly ordered perovskite film with few unintentional defects (Figure 2e) which normally serve as degradation centers.[37]

3. Conclusion

We have demonstrated that the traditional constraints of fabricating efficient $\langle n \rangle = 2$ (according to the precursor stoichiometry) 2D PSCs may be overcome by fully expanding the perovskite phase distribution. The larger difference in organic cation-based colloid size enables a gradually decreased n value distribution from the film surface to the substrate, which improves the energy level alignment and charge transfer in the p-i-n configuration. Employing a high-quality $(NMA)_2(MA)Pb_2I_7$ film with NH_4Cl additive, we implement the first application of $\langle n \rangle = 2$ 2D perovskite in ST-PVs with AVT of 40.5% and PCE of 7.52%. This study highlights new capabilities of low average layer-number 2D perovskites for efficient and stable ST-PV applications, which are likely to be appealing to other perovskite-based optoelectronic devices.

Supporting Information

Supporting Information is available from the Wiley Online Library or from the author.

Conflict of Interest

The authors declare no conflict of interest.

Author Contributions

Y.Y. and C.L. contributed equally to this work. C.L. proposed the research. Y.Y. and C.L. performed the solar cell fabrication, measurement and optimization. Y.Y. conducted the stability tests. H.K. and Y.D. conducted and optimized the GIWAXS. H.H. and H.C. performed and analyzed the TA results. B.D. and P.J.D. contributed to the I-V measurements. Y.L. provided technical support on GIWAXS analysis. X.L. and M.C. performed the PL measurements. Y.D., S.D. and M.K.N. directed this work. Y.Y. and C.L. wrote the first draft of the manuscript. All the authors revised and approved the manuscript.

Data Availability Statement

The data that supports the findings of this study are available in the supplementary material of this article.

[1] C. Sun, R. Xia, H. Shi, H. Yao, X. Liu, J. Hou, F. Huang, H.-L. Yip, Y. Cao, *Joule* **2018**, *2*, 1816.

[2] L. Shen, H.-l. Yip, F. Gao, L. Ding, *Sci. Bull.* **2020**, *65*, 980.

[3] D. Kim, H. J. Jung, I. J. Park, B. W. Larson, S. P. Dunfield, C. Xiao, J. Kim, J. Tong, P. Boonmongkolras, S. G. Ji, *Science* **2020**, *368*, 155.

[4] C. J. Traverse, R. Pandey, M. C. Barr, R. R. Lunt, *Nat. Energy* **2017**, *2*, 849.

[5] B. Shi, L. Duan, Y. Zhao, J. Luo, X. Zhang, *Adv. Mater.* **2020**, *32*, 1806474.

[6] Q. Xue, R. Xia, C. J. Brabec, H.-L. Yip, *Energy Environ. Sci.* **2018**, *11*, 1688.

[7] M. Jeong, I. W. Choi, E. M. Go, Y. Cho, M. Kim, B. Lee, S. Jeong, Y. Jo, H. W. Choi, J. Lee, *Science* **2020**, *369*, 1615.

[8] D. Yang, R. Yang, K. Wang, C. Wu, X. Zhu, J. Feng, X. Ren, G. Fang, S. Priya, S. F. Liu, *Nat. Commun.* **2018**, *9*, 3239.

[9] J.-F. Liao, W.-Q. Wu, Y. Jiang, J.-X. Zhong, L. Wang, D.-B. Kuang, *Chem. Soc. Rev.* **2020**, *49*, 354.

[10] H. Lu, Y. Liu, P. Ahlawat, A. Mishra, W. R. Tress, F. T. Eickemeyer, Y. Yang, F. Fu, Z. Wang, C. E. Avalos, *Science* **2020**, *370*, eabb8985.

[11] Y. Yang, C. Liu, M. Cai, Y. Liao, Y. Ding, S. Ma, X. Liu, M. Guli, S. Dai, M. K. Nazeeruddin, *ACS Appl. Mater. Inter.* **2020**, *12*, 17062.

[12] Y. Wang, T. Mahmoudi, H.-Y. Yang, K. S. Bhat, J.-Y. Yoo, Y.-B. Hahn, *Nano Energy* **2018**, *49*, 59.

[13] C. Roldán-Carmona, O. Malinkiewicz, R. Betancur, G. Longo, C. Momblona, F. Jaramillo, L. Camacho, H. J. Bolink, *Energy Environ. Sci.* **2014**, *7*, 2968.

[14] M. Hörantner, W. Zhang, M. Saliba, K. Wojciechowski, H. Snaith, *Energy Environ. Sci.* **2015**, *8*, 2041.

[15] D. Liu, C. Yang, R. R. Lunt, *Joule* **2018**, *2*, 1827.

[16] Y. Fan, J. Fang, X. Chang, M.-C. Tang, D. Barrit, Z. Xu, Z. Jiang, J. Wen, H. Zhao, T. Niu, *Joule* **2019**, *3*, 2485.

[17] L. Qiu, S. He, L. K. Ono, Y. Qi, *Adv. Energy Mater.* **2020**, *10*, 1902726.

[18] X. Zhang, X. Ren, B. Liu, R. Munir, X. Zhu, D. Yang, J. Li, Y. Liu, D.-M. Smilgies, R. Li, *Energy Environ. Sci.* **2017**, *10*, 2095.

[19] G. Grancini, M. K. Nazeeruddin, *Nat. Rev. Mater.* **2019**, *4*, 4.

[20] Y. Xu, M. Wang, Y. Lei, Z. Ci, Z. Jin, *Adv. Energy Mater.* **2020**, *10*, 2002558.

[21] A. H. Proppe, R. Quintero-Bermudez, H. Tan, O. Voznyy, S. O. Kelley, E. H. Sargent, *J. Am. Chem. Soc.* **2018**, *140*, 2890.

[22] B. Febriansyah, T. M. Koh, Y. Lekina, N. F. Jamaludin, A. Bruno, R. Ganguly, Z. X. Shen, S. G. Mhaisalkar, J. England, *Chem. Mater.* **2019**, *31*, 890.

[23] J. Xi, I. Spanopoulos, K. Bang, J. Xu, H. Dong, Y. Yang, C. D. Malliakas, J. M. Hoffman, M. G. Kanatzidis, Z. Wu, *J. Am. Chem. Soc.* **2020**, *142*, 19705.

[24] H. Pan, X. Zhao, X. Gong, Y. Shen, M. Wang, *J. Phys. Chem. Lett.* **2019**, *10*, 1813.

[25] S. Chen, N. Shen, L. Zhang, W. Kong, L. Zhang, C. Cheng, B. Xu, *J. Mater. Chem. A* **2019**, *7*, 9542.

[26] Y. Yang, C. Liu, A. Mahata, M. Li, C. Roldán-Carmona, Y. Ding, Z. Arain, W. Xu, Y. Yang, P. A. Schouwink, A. Züttel, F. De Angelis, S. Dai, M. K. Nazeeruddin, *Energy Environ. Sci.* **2020**, *13*, 3093.

[27] H. Tsai, W. Nie, J.-C. Blancon, C. C. Stoumpos, R. Asadpour, B. Harutyunyan, A. J. Neukirch, R. Verduzco, J. J. Crochet, S. Tretiak, *Nature* **2016**, *536*, 312.

[28] G. Wu, X. Li, J. Zhou, J. Zhang, X. Zhang, X. Leng, P. Wang, M. Chen, D. Zhang, K. Zhao, *Adv. Mater.* **2019**, *31*, 1903889.

[29] Y. Hu, L. M. Spies, D. Alonso-Álvarez, P. Mocherla, H. Jones, J. Hanisch, T. Bein, P. R. Barnes, P. Docampo, *J. Mater. Chem. A* **2018**, *6*, 22215.

[30] F. Zhang, H. Lu, J. Tong, J. J. Berry, M. C. Beard, K. Zhu, *Energy Environ. Sci.* **2020**, *13*, 1154.

[31] T. He, S. Li, Y. Jiang, C. Qin, M. Cui, L. Qiao, H. Xu, J. Yang, R. Long, H. Wang, *Nat. Commun.* **2020**, *11*, 1672.

[32] R. Yang, R. Li, Y. Cao, Y. Wei, Y. Miao, W. L. Tan, X. Jiao, H. Chen, L. Zhang, Q. Chen, *Adv. Mater.* **2018**, *30*, 1804771.

[33] D. H. Cao, C. C. Stoumpos, O. K. Farha, J. T. Hupp, M. G. Kanatzidis, *J. Am. Chem. Soc.* **2015**, *137*, 7843.

[34] K.-z. Du, Q. Tu, X. Zhang, Q. Han, J. Liu, S. Zauscher, D. B. Mitzi, *Inorg. Chem.* **2017**, *56*, 9291.

[35] Y. Zhang, P. Wang, M.-C. Tang, D. Barrit, W. Ke, J. Liu, T. Luo, Y. Liu, T. Niu, D.-M. Smilgies, *J. Am. Chem. Soc.* **2019**, *141*, 2684.

[36] C. Liu, Y. Yang, O. A. Syzgantseva, Y. Ding, M. A. Syzgantseva, X. Zhang, A. M. Asiri, S. Dai, M. K. Nazeeruddin, *Adv. Mater.* **2020**, *32*, 2002632.

[37] Y. Yang, C. Liu, O. A. Syzgantseva, M. A. Syzgantseva, S. Ma, Y. Ding, M. Cai, X. Liu, S. Dai, M. K. Nazeeruddin, *Adv. Energy Mater.* **2020**, *11*, 2002966.

[38] T. Liu, Y. Jiang, M. Qin, J. Liu, L. Sun, F. Qin, L. Hu, S. Xiong, X. Jiang, F. Jiang, *Nat. Commun.* **2019**, *10*, 878.

[39] F. W. Laird, *J. Phys. Chem.* **2002**, *31*, 1034.

[40] N. Johnston, L. G. Howell, *Phys. Rev.* **1930**, *35*, 274.

[41] S. Zhang, C. Yi, N. Wang, Y. Sun, W. Zou, Y. Wei, Y. Cao, Y. Miao, R. Li, Y. Yin, N. Zhao, J. Wang, W. Huang, *Adv. Mater.* **2017**, *29*, 1606600.

[42] F. Saouma, C. Stoumpos, J. Wong, M. G. Kanatzidis, J. Jang, *Nat. Commun.* **2017**, *8*, 742.

[43] C. C. Stoumpos, D. H. Cao, D. J. Clark, J. Young, J. M. Rondinelli, J. I. Jang, J. T. Hupp, M. G. Kanatzidis, *Chem. Mater.* **2016**, *28*, 2852.

[44] Y. Li, G. Xu, C. Cui, Y. Li, *Adv. Energy Mater.* **2018**, *8*, 1701791.

[45] S.-Y. Chang, P. Cheng, G. Li, Y. Yang, *Joule* **2018**, *2*, 1039.

[46] P. Li, C. Liang, X. L. Liu, F. Li, Y. Zhang, X. T. Liu, H. Gu, X. Hu, G. Xing, X. Tao, *Adv. Mater.* **2019**, *31*, 1901966.

[47] L. K. Ono, Y. Qi, S. F. Liu, *Joule* **2018**, *2*, 1961.

[48] I. Spanopoulos, I. Hadar, W. Ke, Q. Tu, M. Chen, H. Tsai, Y. He, G. Shekhawat, V. P. Dravid, M. R. Wasielewski, *J. Am. Chem. Soc.* **2019**, *141*, 5518.